

# X-ray Underluminous Active Galactic Nuclei Relative to Broad Emission Lines in Ultraluminous Infrared Galaxies

Masatoshi Imanishi <sup>1</sup>

*National Astronomical Observatory, 2-21-1, Osawa, Mitaka, Tokyo 181-8588, Japan*

imanishi@optik.mtk.nao.ac.jp

and

Yuichi Terashima

*The Institute of Space and Astronautical Science, 3-1-1 Yoshinodai, Sagamihara, Kanagawa 226-8510, Japan*

terasima@astro.isas.ac.jp

## ABSTRACT

We present X-ray spectra of four ultraluminous infrared galaxies (ULIRGs) with detectable broad near-infrared emission lines produced by active galactic nuclei (AGNs): Mrk 463, PKS 1345+12, IRAS 05189–2524, and IRAS 07598+6508. With the exception of IRAS 07598+6508, high quality X-ray spectra obtained with *XMM* or *Chandra* show modest (30–340 eV) equivalent widths of the 6.4 keV Fe K $\alpha$  emission line and clear signatures for absorption at a level of 4–33  $\times 10^{22}$  cm<sup>-2</sup> for the main power-law components from the AGNs. These spectral properties are typical of Compton-thin AGNs, and so we estimate absorption-corrected 2–10 keV X-ray luminosities for the AGNs, L<sub>x</sub>(2–10keV), using the Compton-thin assumption. We compare the L<sub>x</sub>(2–10 keV) values with broad optical/near-infrared emission-line luminosities, and confirm a previous finding by Imanishi & Ueno that the L<sub>x</sub>(2–10 keV) to broad-emission-line luminosity ratios in ULIRGs are systematically lower than those of moderately infrared-luminous type-1 AGNs. A comparison of independent energy diagnostic methods

---

<sup>1</sup>Department of Astronomy, School of Science, Graduate University for Advanced Studies, Mitaka, Tokyo 181-8588

suggests that the AGNs are underluminous in the 2–10 keV band with respect to their overall spectral energy distributions, as opposed to the broad emission lines being overluminous. This X-ray under-luminosity should be taken into account when using 2–10 keV X-ray data to investigate the energetic contribution from AGNs to the large infrared luminosities of ULIRGs.

*Subject headings:* galaxies: active — galaxies: nuclei — X-rays: galaxies — galaxies: individual (Mrk 463, IRAS 05189–2524, PKS 1345+12, and IRAS 07598+6508)

## 1. Introduction

The star-formation rate is one of the most important indicators of the nature of a galaxy; it is usually estimated from continuum or emission-line luminosities (Kennicutt 1998). In dusty objects, the infrared luminosity is particularly important, because the correction for dust extinction is generally not significant. An observed infrared luminosity can be converted into a star-formation rate, assuming that the luminosity is powered primarily by star-formation activity. Although this assumption seems to be true in the majority of moderately infrared-luminous galaxies with  $L_{\text{IR}} < 10^{12}L_{\odot}$ , it has been suggested that active galactic nuclei (AGNs) provide an important energetic contribution in ultraluminous infrared galaxies (ULIRGs) with  $L_{\text{IR}} > 10^{12}L_{\odot}$  (Veilleux, Kim, & Sanders 1999a). Therefore, the AGN contribution to the observed infrared luminosity of ULIRGs needs to be properly estimated.

To estimate this contribution, an indicator which can trace AGN power, by disentangling from star-formation activity, is required. Two useful indicators are currently known. The first is the absorption-corrected intrinsic 2–10 keV X-ray luminosity. In an AGN, strong 2–10 keV emission is produced by the inverse-Compton process in the close vicinity of an accretion disk around a central supermassive black hole, whereas the 2–10 keV emission from star-formation is usually much weaker. The second indicator is the broad hydrogen emission lines in the optical and near-infrared domains, whose line widths are larger than  $\sim 1500 \text{ km s}^{-1}$  in full-width at half maximum (FWHM). Such broad emission lines are believed to originate in high-velocity gas (the so-called “broad-line regions”) around a central supermassive black hole in an AGN, rather than being associated with phenomena related to star formation (Veilleux, Sanders, & Kim 1997b). In many dust-unobscured type-1 AGNs with moderate infrared luminosity, both intrinsic 2–10 keV and broad emission-line luminosities have been derived, and a correlation between these luminosities has been found (Ward et al. 1988). If this correlation holds for all types of AGNs, then both of these indicators can be used to estimate AGN’s power in a galaxy.

However, results using *ASCA* data have shown that the absorption-corrected 2–10 keV to broad emission-line luminosity ratios in some ULIRGs are systematically lower than those of dust-unobscured, moderately infrared-luminous, type-1 AGNs (Imanishi & Ueno 1999a). One possible explanation is the large time variability in X-ray luminosity. Some AGNs that were initially classified as X-ray underluminous based on X-ray data taken at one epoch showed normal X-ray luminosities when observed at a later epoch (Risaliti et al. 2003). A second possibility is the misidentification of the origin of the detected 2–10 keV emission. Based on modest equivalent widths of the Fe  $K\alpha$  line at 6.4 keV ( $EW_{6.4} < \text{several} \times 100$  eV) and signatures for Compton-thin absorption ( $N_{\text{H}} < 10^{24} \text{ cm}^{-2}$ ) from *ASCA* spectra, absorption-corrected 2–10 keV luminosities,  $L_{\text{x}}(2\text{--}10 \text{ keV})$ , were derived, assuming that the detected X-ray emission is a direct component from an AGN behind Compton-thin absorbing material (Awaki et al. 1991; Krolik, Madau, & Zycki 1994; Ghisellini, Haardt, & Matt 1994). If, instead, the detected X-ray emission is a scattered/reflected component of AGN emission behind Compton-thick absorbing material ( $N_{\text{H}} > 10^{24} \text{ cm}^{-2}$ ), the intrinsic 2–10 keV luminosity will be larger than the estimate based on the Compton-thin assumption. In the ULIRG, Superantennae, although no significant Fe  $K\alpha$  emission was seen in an *ASCA* spectrum due to limited photon statistics (Imanishi & Ueno 1999b; Pappa, Georgantopoulos, & Stewart 2000), a strong Fe  $K\alpha$  line ( $EW_{6.4} \sim 1.4 \text{ keV}$ ) was reported in a higher quality spectrum obtained later with *XMM* (Braitto et al. 2003a). This demonstrated that the detected 2–10 keV emission is produced by a scattered/reflected component, which was difficult to be recognized based on *ASCA* data. Higher quality *XMM* and *Chandra* data obtained at a different epoch to the *ASCA* era are very useful to (1) investigate whether the X-ray underluminosity of AGNs in ULIRGs found by Imanishi & Ueno (1999a) is caused by X-ray time variability and (2) better understand the origin of detected 2–10 keV emission using higher photon statistics at 2–10 keV and, in particular, near 6.4 keV.

In this paper, we present *XMM* and *Chandra* X-ray spectra of ULIRGs that have detectable broad optical/near-infrared emission lines, in order to investigate the 2–10 keV to broad-line luminosity ratios. Throughout this paper, we adopt  $H_0 = 75 \text{ km s}^{-1} \text{ Mpc}^{-1}$ . Luminosities derived in previous literature using different values of  $H_0$  were re-calculated.  $L_{\text{x}}(2\text{--}10 \text{ keV})$  denotes the absorption-corrected 2–10 keV luminosity of an AGN, unless otherwise stated.

## 2. Targets

Our targets are Mrk 463, PKS 1345+12, IRAS 05189–2524, and IRAS 07598+6508. Table 1 gives detailed information on these sources.

Mrk 463 has a double nucleus with a separation of  $\sim 4$  arcsec at  $1.6 \mu\text{m}$  (Surace & Sanders 1999) and is optically classified as a Seyfert 2 (Sanders et al. 1988). The eastern nucleus (Mrk 463E) is active and shows a broad (FWHM  $> 1500 \text{ km s}^{-1}$ )  $\text{Pa}\beta$  ( $\lambda_{\text{rest}} = 1.28 \mu\text{m}$ ) emission line in the near-infrared (Veilleux, Goodrich, & Hill 1997a). Based on an *ASCA* spectrum, Ueno et al. (1996) estimated an  $\text{EW}_{6.4} < 700 \text{ eV}$ ,  $N_{\text{H}} \sim 2 \times 10^{23} \text{ cm}^{-2}$ , and found the absorption-corrected 2–10 keV luminosity to be  $L_{\text{X}}(2\text{--}10 \text{ keV}) \sim 4 \times 10^{42} \text{ ergs s}^{-1}$ . Mrk 463E was diagnosed to be powered by an AGN, with no detectable star-formation activity in the infrared (Genzel et al. 1998; Veilleux, Sanders, & Kim 1999b; Imanishi 2002). It was found to be underluminous in the 2–10 keV range compared with the [OIII] and broad optical/near-infrared line emission (Ueno et al. 1996; Imanishi & Ueno 1999a).

PKS 1345+12 is a double-nucleus source with a separation of  $\sim 2$  arcsec, with the western nucleus  $\sim 3$  times brighter at  $2 \mu\text{m}$  than the eastern nucleus (Surace & Sanders 1999). It is optically classified as a Seyfert 2 (Sanders et al. 1988), and shows a broad  $\text{Pa}\alpha$  ( $\lambda_{\text{rest}} = 1.88 \mu\text{m}$ ) emission line in the near-infrared (Veilleux et al. 1997b). Imanishi & Ueno (1999b) estimated an  $\text{EW}_{6.4} < 500 \text{ eV}$ ,  $N_{\text{H}} = 1\text{--}4 \times 10^{22} \text{ cm}^{-2}$ , and  $L_{\text{X}}(2\text{--}10 \text{ keV}) \sim 3 \times 10^{43} \text{ ergs s}^{-1}$ , based on an *ASCA* spectrum. This source is thought to be powered by an AGN (Veilleux et al. 1999b). It was found to be underluminous in 2–10 keV X-rays, compared to the broad optical/near-infrared emission-line luminosity (Imanishi & Ueno 1999a).

IRAS 05189–2524 is a single-nucleus source (Sanders et al. 1988), optically classified as a Seyfert 2 (Veilleux et al. 1999a), and shows a broad  $\text{Pa}\alpha$  emission line (Veilleux et al. 1999b). Severgnini et al. (2001) later reported the presence of broad components of  $\text{Pa}\beta$  and  $\text{Pa}\alpha$  emission lines, and argued that the broad  $\text{H}\alpha$  ( $\lambda_{\text{rest}} = 0.65 \mu\text{m}$ ) component detected in the previous optical spectrum (Young et al. 1996) is a transmitted component, rather than a scattered/reflected component. This source was not included in Imanishi & Ueno (1999a), but Severgnini et al. (2001) later presented *ASCA* and *BeppoSAX* X-ray spectra which show  $\text{EW}_{6.4} \sim 100\text{--}150 \text{ eV}$ ,  $N_{\text{H}} = 4\text{--}9 \times 10^{22} \text{ cm}^{-2}$ , and  $L_{\text{X}}(2\text{--}10 \text{ keV}) \sim 2 \times 10^{43} \text{ ergs s}^{-1}$ . From the  $L_{\text{X}}(2\text{--}10 \text{ keV})$  value, Severgnini et al. (2001) argued that the AGN is not powerful enough to account for the bulk of the infrared luminosity. However, some independent diagnostics in the infrared suggested that this source is dominated by an AGN (Veilleux et al. 1999b; Soifer et al. 2000; Imanishi & Dudley 2000).

IRAS 07598+6508 is a single-nucleus source, optically classified as a Seyfert 1 (Sanders et al. 1988), shows a broad  $\text{Pa}\alpha$  emission line (Taniguchi et al. 1994), and is a member of the class of broad absorption line (BAL) quasars (Lipari 1994; Hines & Wills 1995). No X-ray emission was detected by *ASCA* (Risaliti et al. 2000).

### 3. Observations and Data Analysis

#### 3.1. XMM

Mrk 463, IRAS 05189–2524, and IRAS 07598+6508 were observed with the EPIC cameras (PN, MOS1, and MOS2) on board *XMM*, in full-frame mode. Observing details are shown in Table 1. Standard data analysis procedures were employed, using the *XMM* Science Analysis System (SAS version 5.4), together with standard software packages (FTOOLS 5.2 and XSPEC 11.2). Events recorded during high-background time intervals were removed, and only events corresponding to pattern 0–4 for PN and pattern 0–12 for MOS were included in the analysis. The most recent calibration files retrieved from the XMM webpage and response matrices created with SAS were used for the data analysis.

The source spectra of Mrk 463 and IRAS 05189–2524 were extracted from 30 arcsec radius circular regions, whereas for IRAS 07598+6508 a 22.5 arcsec circle was used. Background spectra were extracted from nearby source-free circular regions of 60 arcsec radius. Spectra were binned so that each energy channel had more than 20 counts. Since the PN spectra have the best photon statistics, they were used for primary estimation of important parameters. However, to improve the statistics, final spectral fitting was performed using a combination of PN, MOS1, and MOS2, keeping the relative normalization free, because there is some uncertainty about the relative flux calibration of the three cameras.

#### 3.2. Chandra

PKS 1345+12 was observed with *Chandra*. Table 1 summarizes the observing information. A 1/8 sub-array mode of the ACIS-S3 back-illuminated CCD chip was used, with a 0.4-sec frame time. The data were reprocessed with CIAO 2.2.1 and CALDB 2.17. Only *ASCA* (“good”) grades 0, 2, 3, 4, and 6 were used in the analysis. High background intervals were removed.

A nuclear spectrum was extracted from a circular region with a radius of 8 arcsec. A background spectrum was extracted from an annular region around the nucleus, and subtracted from the nuclear spectrum. The count rate from the nucleus was 0.057 counts  $\text{s}^{-1}$ , and the effect of pileup was negligible.

#### 4. Results

All sources are clearly detected in the *XMM* or *Chandra* images. For PKS 1345+12, the high resolution *Chandra* image reveals that the X-ray emission comes from the western nucleus (Figure 1). Figure 2 shows *XMM* EPIC spectra of Mrk 463, IRAS 05189–2524, and IRAS 07598+6508, and a *Chandra* spectrum of PKS 1345+12.

In the X-ray spectra of Mrk 463, PKS 1345+12, and IRAS 05189–2524, an absorbed hard component is clearly seen at  $>2$  keV. This hard component is likely to originate in the AGN, and so is fitted with an absorbed power law. In addition to this hard component, there exists a soft X-ray component which dominates the emission at  $<2$  keV. There are two physically plausible explanations for the origin of the soft X-ray emission: (1) a scattered/reflected component of the primary AGN power-law emission, and (2) emission from a starburst. In the caption of Table 2, detailed descriptions of the models used are reported for each source.

For the spectral fitting of Mrk 463, a single temperature thermal component (from a starburst) or a second power law (a Thomson-scattered component of the primary power law emission from the AGN and/or X-ray binaries in a starburst) was initially included, in addition to the main absorbed power-law component. However, significant residuals remained at  $<2$  keV. We then tried model (A), a low-temperature (0.5–1 keV) thermal model + a high-temperature (5–10 keV) thermal component (from hot gas and X-ray binaries originating in a starburst), and model (B), a single-temperature (0.5–1 keV) thermal model + second power law. In addition, since emission lines are seen at 6.5–7.0 keV, narrow Gaussians at 6.4 keV, 6.7 keV, and 7.0 keV,  $K\alpha$  emission lines from Fe at different ionized levels, were also included in the model fitting. Table 2 summarizes the best-fit models that were adopted. The  $L_X(2-10$  keV) depends only weakly on the adopted models. We obtained  $EW_{6.4} \sim 340$  eV,  $N_H \sim 3 \times 10^{23}$  cm $^{-2}$ , and  $L_X(2-10$  keV)  $\sim 9 \times 10^{42}$  ergs s $^{-1}$  in both models. The  $L_X(2-10$  keV) is about twice as large as the estimate based on *ASCA* data (Ueno et al. 1996). The absorption-corrected 2–10 keV X-ray to observed infrared luminosity ratio is  $L_X(2-10$  keV)/ $L_{IR} \sim 5 \times 10^{-3}$ .

For PKS 1345+12, a second power law and a narrow Gaussian (6.4 keV Fe  $K\alpha$  line) were included, in addition to the main absorbed power-law component (model C). The X-ray spectrum is well fitted (Table 2). We obtained  $EW_{6.4} \sim 130$  eV,  $N_H \sim 5 \times 10^{22}$  cm $^{-2}$ , and  $L_X(2-10$  keV)  $\sim 4 \times 10^{43}$  ergs s $^{-1}$ . The  $L_X(2-10$  keV) we obtain is about 30% higher than that derived from *ASCA* data (Imanishi & Ueno 1999b).  $L_X(2-10$  keV)/ $L_{IR}$  is  $\sim 6 \times 10^{-3}$ .

For IRAS 05189–2524, model (D), a low temperature (0.5–1 keV) thermal model + an even lower temperature ( $<0.3$  keV) second thermal component, and model (E), a single-

temperature ( $<1$  keV) thermal model + second power-law component, were used, primarily to account for the soft X-ray emission. A narrow Gaussian for the Fe  $K\alpha$  line at 6.4 keV was also added, although this line is not as clear as in Mrk 463. Table 2 summarizes the adopted best-fit models. We obtained  $EW_{6.4} \sim 30$  eV,  $N_H \sim 6 \times 10^{22}$  cm $^{-2}$ , and  $L_x(2-10$  keV)  $\sim 2 \times 10^{43}$  ergs s $^{-1}$ . The  $L_x(2-10$  keV) agrees with the *ASCA* and *BeppoSAX* estimates (Severgnini et al. 2001).  $L_x(2-10$  keV)/ $L_{IR}$  is  $\sim 4 \times 10^{-3}$ .

IRAS 07598+6508 shows no clear signature for an absorbed hard component. The spectrum was fitted with a primary power law and a narrow Gaussian for the Fe  $K\alpha$  6.4 keV line (Table 2). Although no strong Fe  $K\alpha$  line is evident at 6.4 keV,  $EW_{6.4}$  could not be constrained strongly ( $EW_{6.4} < 13$  keV), due to poor photon statistics.  $L_x(2-10$  keV) and  $L_x(2-10$  keV)/ $L_{IR}$  are estimated to be  $\sim 8 \times 10^{41}$  ergs s $^{-1}$  and  $\sim 9 \times 10^{-5}$ , respectively. BAL quasars are known to be weaker X-ray emitters than non-BAL quasars, due to absorption (Green et al. 2001). The substantially smaller  $L_x(2-10$  keV)/ $L_{IR}$  in IRAS 07598+6508 (BAL quasar) than the other three ULIRGs may be related to the BAL phenomena. The best fit value for the power law index  $\Gamma \sim 2.9$  (Table 2) is larger than the canonical value for AGNs ( $\Gamma \sim 1.8-2.0$ ). The large  $\Gamma$  value may be caused by the presence of additional soft X-ray emission which can steepen the apparent X-ray spectrum. However, the limited photon statistics hamper more detailed investigations of the spectrum.

## 5. Discussion

### 5.1. The 2–10 keV to Broad Line Luminosity Ratio

For Mrk 463, PKS 1345+12, and IRAS 05189–2524, the modest  $EW_{6.4}$  ( $< \text{several} \times 100$  eV) and clear signatures for absorption with  $N_H < \text{several} \times 10^{23}$  cm $^{-2}$  suggest that the detected hard component is direct emission from an AGN behind Compton-thin absorbing material (Awaki et al. 1991; Krolik, Madau, & Zycki 1994; Ghisellini, Haardt, & Matt 1994), and so the absorption-corrected 2–10 keV luminosities,  $L_x(2-10$  keV), estimated in §4, can be taken as the intrinsic X-ray luminosity of the AGN. Therefore, the 2–10 keV to broad-line luminosity ratios for the AGNs in these ULIRGs can be compared with those for moderately infrared-luminous type-1 AGNs (Ward et al. 1988). For IRAS 07598+6508, however, the constraint on  $EW_{6.4}$  ( $<13$  keV) is so loose that it is unclear whether the observed 2–10 keV flux is a direct component behind Compton-thin absorbing material ( $EW_{6.4} < \text{several} \times 100$  eV). The extremely small  $L_x(2-10$  keV)/ $L_{IR}$  ratio and small  $N_H$  ( $\sim 8 \times 10^{20}$  cm $^{-2}$ ) suggest that the observed 2–10 keV emission is a scattered/reflected component behind Compton-thick absorbing material. This source will be excluded from the following discussions.

The correlation between 2–10 keV and broad emission lines established for type-1 AGNs (Ward et al. 1988) is for the broad component of an optical  $H\alpha$  ( $\lambda_{\text{rest}} = 0.65 \mu\text{m}$ ) emission line. Thus, we need to convert the luminosity of a broad near-infrared emission line ( $\text{Pa}\alpha$  for PKS 1345+12 and IRAS 05189–2524 <sup>2</sup>; Veilleux et al. 1997b,1999b, and  $\text{Pa}\beta$  for Mrk 463; Veilleux et al. 1997a) to that of broad  $H\alpha$ . For emission lines from the broad-line regions in an AGN, the case-B assumption is not applicable to low-level transition lines, such as  $H\alpha$ , due to collisional effects (Osterbrock 1989). For the broad  $H\alpha$  to  $\text{Pa}\alpha$  luminosity ratio, the value of 20 observed in dust-unobscured type-1 AGNs (Hill et al. 1996) was adopted. Since the deviation of this ratio from case-B ( $\sim 10$ ) is only a factor of  $\sim 2$ , the choice of this ratio will not affect our main conclusions significantly. For high-transition broad emission lines, such as  $\text{Pa}\alpha$  and  $\text{Pa}\beta$ , case-B is applicable (Rhee & Larkin 2000). Thus, a broad  $\text{Pa}\alpha$  to  $\text{Pa}\beta$  luminosity ratio of 1.9 (case-B) was adopted.

Absorption-*corrected* 2–10 keV and extinction-*uncorrected* broad emission-line luminosities for the three ULIRGs are plotted in Figure 3 (solid squares), where the estimated broad  $H\alpha$  emission-line luminosities are  $\sim 5$ ,  $\sim 3$ , and  $\sim 1 \times 10^{43}$  ergs  $\text{s}^{-1}$  for Mrk 463, PKS 1345+12, and IRAS 05189–2524, respectively. The type-1 AGNs studied by Ward et al. (1988) are plotted for comparison (open circles). In addition to the three ULIRGs, the other two Seyfert-2 ULIRGs with detectable broad near-infrared  $\text{Pa}\alpha$  emission lines, IRAS 20460+1925 and IRAS 23060+0505 (Veilleux et al. 1997b), have available *ASCA* 2–10 keV spectra (Ogasaka et al. 1997; Brandt et al. 1997). Since their observed 2–10 keV fluxes are sufficiently high ( $> 10^{-12}$  ergs  $\text{s}^{-1} \text{cm}^{-2}$ ), strong constraints were obtained for  $\text{EW}_{6.4}$  ( $260_{-137}^{+145}$  eV for IRAS 20460+1925; Ogasaka et al. 1997,  $< 290$  eV for IRAS 23060+0505; Brandt et al. 1997). The detected 2–10 keV fluxes show signatures for absorption with  $N_{\text{H}} = 2\text{--}8 \times 10^{22} \text{cm}^{-2}$ , so that the detected 2–10 keV flux is taken as a direct component from an AGN behind Compton-thin absorbing material. For IRAS 20460+1925,  $L_{\text{x}}(2\text{--}10 \text{ keV})$  is  $\sim 1 \times 10^{44}$  ergs  $\text{s}^{-1}$  (Ogasaka et al. 1997) and  $L_{\text{x}}(2\text{--}10 \text{ keV})/L_{\text{IR}}$  is  $\sim 1 \times 10^{-2}$ . For IRAS 23060+0505,  $L_{\text{x}}(2\text{--}10 \text{ keV})$  is  $\sim 2 \times 10^{44}$  ergs  $\text{s}^{-1}$  (Brandt et al. 1997) and  $L_{\text{x}}(2\text{--}10 \text{ keV})/L_{\text{IR}}$  is  $\sim 2 \times 10^{-2}$ . Broad  $H\alpha$  emission-line luminosities were derived from  $\text{Pa}\alpha$  data (Veilleux et al. 1997b) using the method described above and estimated to be  $\sim 2$  and  $\sim 1 \times 10^{44}$  ergs  $\text{s}^{-1}$  for IRAS 20460+1925 and IRAS 23060+0505, respectively. These two ULIRGs are also plotted in Fig. 3 (solid squares). The five Seyfert-2 ULIRGs show absorption-*corrected* 2–10 keV to extinction-*uncorrected* broad line luminosity ratios roughly an order of magnitude smaller than those in dust-unobscured type-1 AGNs with modest infrared luminosities. While no significant dust extinction is expected for broad emission lines in type-1 AGNs,

---

<sup>2</sup>In IRAS 05189–2524, broad components were detected at  $H\alpha$ ,  $\text{Pa}\beta$ , and  $\text{Pa}\alpha$  (see § 2). We use the  $\text{Pa}\alpha$  line, because dust extinction is the lowest.



some degree of dust extinction may be present for the five Seyfert-2 ULIRGs. For these five ULIRGs, since near-infrared Pa $\alpha$  or Pa $\beta$  emission lines were used to estimate the broad H $\alpha$  luminosities, the effects of dust extinction are expected to be reduced. If some amount of dust extinction is present for the broad near-infrared emission lines and its correction is applied, these five ULIRGs will move to the right in Fig. 3, making the deviation of these ULIRGs even larger. Even using new *XMM* and *Chandra* data, we confirmed systematically smaller 2–10 keV to broad line luminosity ratios in ULIRGs, originally suggested by Imanishi & Ueno (1999a).

It is unlikely that the systematic difference is caused by the uncertainty of the luminosity conversion from broad Pa $\alpha$  or Pa $\beta$  to H $\alpha$  for the following two reasons. First, in a number of moderately infrared-luminous type-2 AGNs, the 2–10 keV to broad-H $\alpha$  luminosity ratios derived from observed broad near-infrared line luminosities agree with those for unobscured type-1 AGNs (Imanishi & Ueno 1999a). Second, for IRAS 05189–2524, the intrinsic broad H $\alpha$  luminosity estimated from the observed broad Pa $\alpha$  luminosity ( $L_{\text{H}\alpha} \sim 1 \times 10^{43}$  ergs s $^{-1}$ ; see previous paragraph) is in good agreement with that derived directly from the broad H $\alpha$  luminosity (Young et al. 1996) after correction for dust extinction estimated by Severgnini et al. (2001) is applied ( $L_{\text{H}\alpha} \sim 1 \times 10^{43}$  ergs s $^{-1}$ ). Both of these results suggest that (1) the luminosity conversion from broad near-infrared emission lines to broad H $\alpha$  is reasonable, and that (2) at least for some sources with detectable broad near-infrared emission lines, dust extinction is not significant in the near-infrared domain. Thus, the significant deviation of ULIRGs in Fig. 3 is believed to be real.

## 5.2. X-ray Underluminous or Broad Line Overluminous?

Estimating the fractional AGN contribution to the large infrared luminosities of ULIRGs is of particular importance to the study of their energy sources. It is not clear which of the two AGN indicators, 2–10 keV emission or broad optical/near-infrared emission lines, is a better tracer of this fraction. The 2–10 keV luminosity depends primarily on the number of hot electrons in the close vicinity of an accretion disk around a central supermassive blackhole in an AGN and the number of incident UV photons to be Compton up-scattered. The broad emission-line luminosity is roughly proportional to the product of the number of UV photons from the central AGN and the covering factor of broad-line gas clouds. The infrared luminosity of a ULIRG powered by an AGN is determined mainly by the number of UV photons from the AGN and by the covering factor of dust. In the nuclear region of a ULIRG, a large amount of gas and dust is available (Sanders & Mirabel 1996), which may increase the covering factors both of dust and broad-line gas clouds around the AGN.

If this is the case, broad emission lines are a better indicator of the AGN’s contribution to the infrared luminosity, and AGNs in ULIRGs are underluminous in 2–10 keV X-rays.

In fact, in a number of ULIRGs, although an AGN is consistently suggested to be the primary energy source by some independent methods, only energy diagnostics based on the 2–10 keV luminosity suggest that the AGN is energetically insufficient. Examples include IRAS 05189–2524 (Veilleux et al. 1999b; Soifer et al. 2000; Imanishi & Dudley 2000; Severgnini et al. 2001) and Mrk 463 (Ueno et al. 1996; Genzel et al. 1998; Imanishi 2002). Thus, it is more likely that the AGNs in ULIRGs are underluminous in X-rays with respect to their overall spectral energy distributions, than that their broad lines are overluminous.

If X-ray underluminosity (relative to UV) is an intrinsic property of ULIRGs, one possible explanation is a high mass accretion rate onto a central supermassive black hole (Bechtold et al. 2003). This is plausible in ULIRGs, given the high nuclear concentration of gas and dust (Sanders & Mirabel 1996).

Alternatively, the apparent X-ray underluminosity of AGNs in ULIRGs may be caused by our misidentification of the origin of the detected 2–10 keV emission from ULIRGs. Using reasonable assumptions for an AGN, the scattered/reflected X-ray component of AGN emission behind Compton-thick absorbing material is expected to show a very large  $EW_{6.4}$  with  $>1$  keV and only weak absorption (Matt, Guainazzi, & Maiolino 2003). A modest  $EW_{6.4}$  and clear Compton-thin absorption signature, as were found in the five ULIRGs, make it most plausible that we are observing direct X-ray emission from an AGN behind Compton-thin absorbing material (Awaki et al. 1991; Krolik, Madau, & Zycki 1994; Ghisellini, Haardt, & Matt 1994). However, Thomson scattering by highly ionized gas produces a small  $EW_{6.4}$ . If the scattered component suffers some degree of absorption, both the modest  $EW_{6.4}$  and clear signature for Compton-thin absorption can be explained (Maloney & Reynolds 2000). In this scenario, the intrinsic 2–10 keV luminosity of an AGN could be substantially larger, depending on the scattering efficiency. Since such X-ray spectra are usually interpreted as Compton-thin, and the absorption-corrected 2–10 keV luminosity is determined based on this assumption, we will underestimate the true  $L_x(2-10 \text{ keV})$ .

A third possibility which could explain the observed X-ray underluminosity is partial Compton-thick X-ray absorption. If the X-ray-absorbing material in front of an AGN consists of small clumps of Compton-thick and thin clouds, whose size scales are substantially smaller than the size of the X-ray-emitting region of the AGN, then the 2–10 keV spectrum will suggest Compton-thin absorption. The actual  $L_x(2-10 \text{ keV})$  could be significantly larger than a simple estimate assuming uniform Compton-thin X-ray absorption. The covering factor of Compton-thick clouds in front of an AGN along our line-of-sight determines the degree of our underestimate for  $L_x(2-10 \text{ keV})$ , but an X-ray spectrum at  $>10$  keV is required

to determine this (Braitto et al. 2003b).

Whether the X-ray underluminosity of AGNs in ULIRGs is intrinsic or caused by our underestimate of  $L_x(2\text{--}10\text{ keV})$ , the use of 2–10 keV observations to estimate AGNs’ contribution to the infrared luminosities of ULIRGs will be quite misleading, unless the X-ray underluminosity is properly taken into account.

The discovery of underluminous X-ray emission relative to broad emission lines from AGNs is only for ULIRGs with modest dust obscuration along our sightlines, because in order for broad optical/near-infrared emission lines to be detected, dust obscuration toward AGNs must be relatively low. The putative AGNs in the majority of ULIRGs are so highly dust-obscured that broad emission lines are not detectable (Veilleux et al. 1999b), and so we have no information on the broad line luminosities. It is unclear whether X-ray underluminosity is a general property of AGNs in the majority of ULIRGs, and there is currently no way to determine this. However, when using 2–10 keV data to determine the energy contribution of AGNs in ULIRGs, it is important to consider that the AGN contribution may be significantly underestimated.

## 6. Summary

We estimated the absorption-corrected 2–10 keV X-ray luminosities of AGNs in moderately dust-obscured ULIRGs, and confirmed a previous finding that absorption-*corrected* 2–10 keV to extinction-*uncorrected* broad emission-line luminosity ratios in ULIRGs are roughly an order of magnitude smaller than those of type-1 AGNs with modest infrared luminosities. We have shown that the smaller ratios are more likely to be due to 2–10 keV X-ray underluminosity with respect to the overall spectral energy distributions, rather than higher broad-emission-line luminosity. The lower X-ray luminosities of AGNs in ULIRGs should be taken into account in estimating AGNs’ contribution to the energy output from ULIRGs based on X-ray data.

Y.T. acknowledges the Research Fellowship of the Japan Society for the Promotion of Science for Young Scientists. This work is based on observations obtained with XMM-Newton, an ESA science mission with instruments and contributions directly funded by ESA Member States and the USA (NASA), and with Chandra. This research has made use of the SIMBAD database, operated at CDS, Strasbourg, France, and of the NASA/IPAC Extragalactic Database (NED) which is operated by the Jet Propulsion Laboratory, California Institute of Technology, under contract with the National Aeronautics and Space Administration.

## REFERENCES

- Awaki, H., Koyama, K., Inoue, H., & Halpern, J. P. 1991, PASJ, 43, 195
- Bechtold, J. et al. 2003, ApJ, 588, 119
- Braito, V. et al. 2003a, A&A, 398, 107
- Braito, V. et al. 2003b, astro-ph/0307551
- Brandt, W. N., Fabian, A. C., Takahashi, K., Fujimoto, R., Yamashita, A., Inoue, H., & Ogasaka, Y. 1997, MNRAS, 290, 617
- Evans, A. S., Kim, D. C., Mazzarella, J. M., Scoville, N. Z., & Sanders, D. B. 1999, ApJ, 521, L107
- Genzel, R. et al. 1998, ApJ, 498, 579
- Ghisellini, G., Haardt, F., & Matt, G. 1994, MNRAS, 267, 743
- Green, P. J., Aldcroft, T. L., Mathur, S., Wilkes, B. J., & Elvis, M. 2001, ApJ, 558, 109
- Hill, G. J., Goodrich, R. W., & Depoy, D. L. 1996, ApJ, 462, 163
- Hines, D. C., & Wills, B. J. 1995, ApJ, 448, L69
- Imanishi, M. 2002, ApJ, 569, 44
- Imanishi, M., & Ueno, S. 1999a, MNRAS, 305, 829
- Imanishi, M., & Ueno, S. 1999b, ApJ, 527, 709
- Imanishi, M., & Dudley, C. C. 2000, ApJ, 545, 701
- Kennicutt, R. C. Jr. 1998, ARA&A, 36, 189
- Krolik, J. H., Madau, P., Zycki, P. T. 1994, ApJ, 420, L57
- Lipari, S. 1994, ApJ, 436, 102
- Maloney, P. R., & Reynolds, C. S. 2000, ApJ, 545, L23
- Matt, G., Guainazzi, M., & Maiolino, R. 2003, MNRAS, 342, 422
- Ogasaka, Y., Inoue, H., Brandt, W. N., Fabian, A. C., Kii, T., Nakagawa, T., Fujimoto, R., & Otani, C. 1997, PASJ, 49, 179

- Osterbrock, D. E. 1989, *Astrophysics of Gaseous Nebulae and Active Galactic Nuclei* (Cambridge: Cambridge Univ. Press)
- Pappa, A., Georgantopoulos, I., & Stewart, G. C. 2000, *MNRAS*, 314, 589
- Rhee, J. H., & Larkin, J. E. 2000, *ApJ*, 538, 98
- Risaliti, G., Gilli, R., Maiolino, R., & Salvati, M. 2000, *A&A*, 357, 13
- Risaliti, G., Elvis, M., Gilli, R., & Salvati, M. 2003, *ApJ*, 587, L9
- Sanders, D. B., Soifer, B. T., Elias, J. H., Neugebauer, G., & Matthews, K. 1988, *ApJ*, 328, L35
- Sanders, D. B., & Mirabel, I. F. 1996, *ARA&A*, 34, 749
- Severgnini, P., Risaliti, G., Marconi, A., Maiolino, R., & Salvati, M. 2001, *A&A*, 368, 44
- Soifer, B. T. et al. 2000, *AJ*, 119, 509
- Surace, J. A., & Sanders, D. B. 1999, *ApJ*, 512, 162
- Taniguchi, Y., Kawara, K., Murayama, T., & Sato, Y. 1994, *AJ*, 107, 1668
- Ueno, S., Koyama, K., Awaki, H., Hayashi, I., & Blanco, P. R. 1996, *PASJ*, 48, 389
- Veilleux, S., Goodrich, R. W., & Hill, G. J. 1997a, *ApJ*, 477, 631
- Veilleux, S., Sanders, D. B., & Kim, D. -C. 1997b, *ApJ*, 484, 92
- Veilleux, S., Kim, D. -C., & Sanders, D. B. 1999a, *ApJ*, 522, 113
- Veilleux, S., Sanders, D. B., & Kim, D. -C. 1999b, *ApJ*, 522, 139
- Ward, M. J., Done, C., Fabian, A. C., Tennant, A. F., & Shafer, R. A. 1988, *ApJ*, 324, 767
- Young, S. et al. 1996, *MNRAS*, 281, 1026

Table 1. Details of Observed ULIRGs.

Object	$z$	$L_{\text{IR}}$ [ergs s <sup>-1</sup> ]	Satellite	Date [UT]	Net Exposure [ksec]
(1)	(2)	(3)	(4)	(5)	(6)
Mrk 463	0.051	45.3 <sup>1</sup>	XMM	2001 Dec 22	21 (PN), 25 (MOS)
PKS 1345+12	0.122	45.8	Chandra	2000 Feb 24	19
IRAS 05189–2524	0.042	45.7	XMM	2001 Mar 17	7 (PN), 10 (MOS)
IRAS 07598+6508	0.149	46.0	XMM	2001 Oct 25	13 (PN), 19 (MOS)

Note. — Column (1): Object. Column (2): Redshift. Column (3): Logarithm of infrared (8–1000  $\mu\text{m}$ ) luminosity in ergs s<sup>-1</sup> calculated with  $L_{\text{IR}} = 2.1 \times 10^{39} \times D(\text{Mpc})^2 \times (13.48 \times f_{12} + 5.16 \times f_{25} + 2.58 \times f_{60} + f_{100})$  ergs s<sup>-1</sup> (Sanders & Mirabel 1996), where  $f_{12}$ ,  $f_{25}$ ,  $f_{60}$ , and  $f_{100}$  are *IRAS FSC* fluxes at 12 $\mu\text{m}$ , 25 $\mu\text{m}$ , 60 $\mu\text{m}$ , and 100 $\mu\text{m}$ , respectively. Column (4): X-ray satellite used for the observation. Column (5): Observing date in UT. Column (6): Effective exposure time in ksec after discarding high background intervals.

<sup>1</sup>Mrk 463 is not a ULIRG in the strict sense, but is included, since its infrared luminosity is close to that of a ULIRG.

Table 2. Results of X-ray Spectral Fitting.

Object	Model <sup>1</sup>	$\chi^2/\text{d.o.f.}$	$N_{\text{H}}$ [ $10^{22} \text{ cm}^{-2}$ ]	$L_{\text{X}}(2\text{--}10\text{keV})$ [ $10^{42} \text{ ergs s}^{-1}$ ]	$\text{EW}_{6.4}$ [eV]
(1)	(2)	(3)	(4)	(5)	(6)
Mrk 463	A	231.6/202	$33_{-6}^{+3}$	9.2	$340_{-100}^{+70}$
	B	230.4/203	$32 \pm 3$	9.1	$340_{-90}^{+70}$
PKS 1345+12	C	49.2/62	$4.5_{-0.4}^{+0.5}$	38	$130 \pm 130$
IRAS 05189–2524	D	225.9/232	$5.7 \pm 0.3$	17	$30_{-30}^{+50}$
	E	233.2/233	$5.8 \pm 0.4$	16	$30_{-30}^{+50}$
IRAS 07598+6508	F	25.1/23	$0.08_{-0.06}^{+0.10}$	0.8	<13000

Note. — Column (1): Object. Column (2): Adopted best-fit models. Column (3): Reduced  $\chi^2$  values. Column (4): Absorption for the main power law component. The uncertainty is at 90% confidence level for one parameter of interest ( $\Delta\chi^2 = 2.7$ ) throughout this Table. Column (5): Absorption-corrected 2–10 keV X-ray luminosity for the main power law component, estimated based on the assumption of uniform Compton-thin absorption. Column (6): Equivalent width of the 6.4 keV Fe  $K\alpha$  emission line relative to the main power law component.

<sup>1</sup> Model A : absorbed power law ( $\Gamma = 1.8$  fixed) + thermal (kT =  $0.6 \pm 0.1$  keV) + thermal (kT = 10 keV fixed) + narrow Gaussian (6.4 keV Fe  $K\alpha$ ) + narrow Gaussian (6.7 keV, EW =  $30_{-30}^{+50}$  eV) + narrow Gaussian (7.0 keV, EW =  $120_{-70}^{+100}$  eV)

Model B : absorbed power law ( $\Gamma = 1.8$  fixed) + thermal (kT =  $0.6 \pm 0.1$  keV) + second power law ( $\Gamma = 1.8$  fixed;  $\sim 5\%$  of the main power law component in normalization) + narrow Gaussian (6.4 keV Fe  $K\alpha$ ) + narrow Gaussian (6.7 keV, EW =  $40_{-40}^{+50}$  eV) + narrow Gaussian (7.0 keV, EW =  $130 \pm 80$  eV)

Model C : absorbed power law ( $\Gamma = 1.8$  fixed) + second power law ( $\Gamma = 1.8$  fixed;  $\sim 3\%$  of the main power law component in normalization) + narrow Gaussian (6.4 keV Fe  $K\alpha$ )

Model D : absorbed power law ( $\Gamma = 1.8$  fixed) + thermal (kT =  $0.7_{-0.2}^{+0.1}$  keV) + thermal (kT =  $0.11 \pm 0.02$  keV) + narrow Gaussian (6.4 keV Fe  $K\alpha$ )

Model E : absorbed power law ( $\Gamma = 1.8$  fixed) + thermal (kT =  $0.3 \pm 0.1$  keV) + second power law ( $\Gamma = 1.8$  fixed;  $\sim 1\%$  of the main power law component in normalization) + narrow Gaussian (6.4 keV Fe  $K\alpha$ )

Model F : absorbed power law ( $\Gamma = 2.9_{-0.5}^{+0.6}$ ) + narrow Gaussian (6.4 keV Fe  $K\alpha$ )

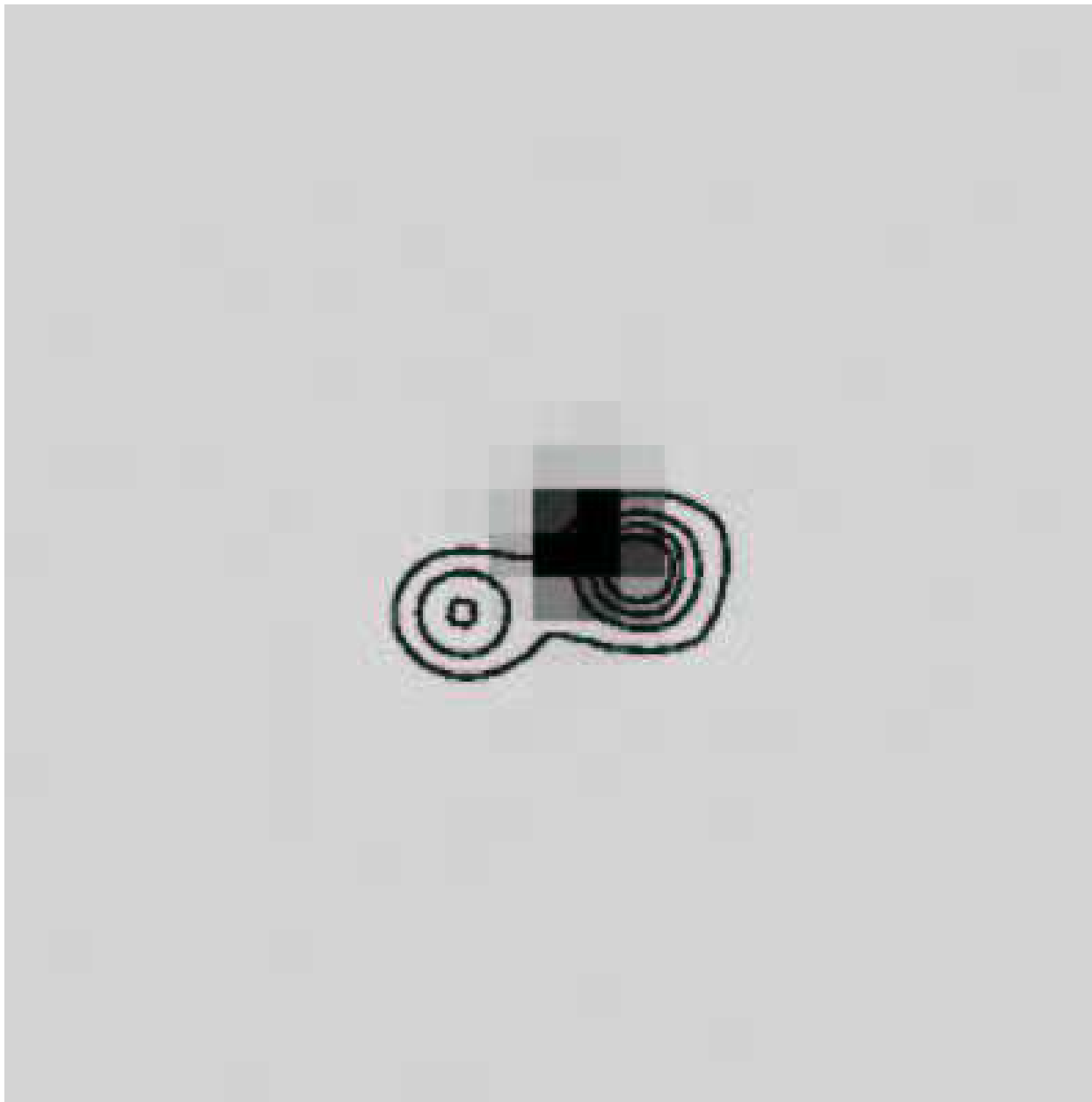


Fig. 1.— A *Chandra* 0.5–8 keV X-ray image of PKS 1345+12, with infrared 2.2- $\mu\text{m}$  contours obtained from archival *HST* NICMOS data overplotted. North is up and east is to the left. The field of view is  $12 \times 12$  arcsec<sup>2</sup>. The contours from the lowest one are 12.5%, 25%, 50%, and 100% of the highest level at the western nucleus. The coordinate of the X-ray emission peak in this *Chandra* image is J2000.0[13:47:33.37, 12:17:24.3], which is slightly displaced from the 2.2- $\mu\text{m}$  peak of the western nucleus estimated from the NICMOS archival data (J2000.0[13:47:33.33, 12:17:24.0]). Evans et al. (1999) made more accurate astrometry of this galaxy, and estimated the coordinate of the 2.2  $\mu\text{m}$  peak of the western nucleus to be J2000.0[13:47:33.38, 12:17:24.4]. Considering the absolute positional uncertainty of *Chandra* (0.6 arcsec for 90% error radius), we conclude that the X-ray emission comes from the western nucleus.



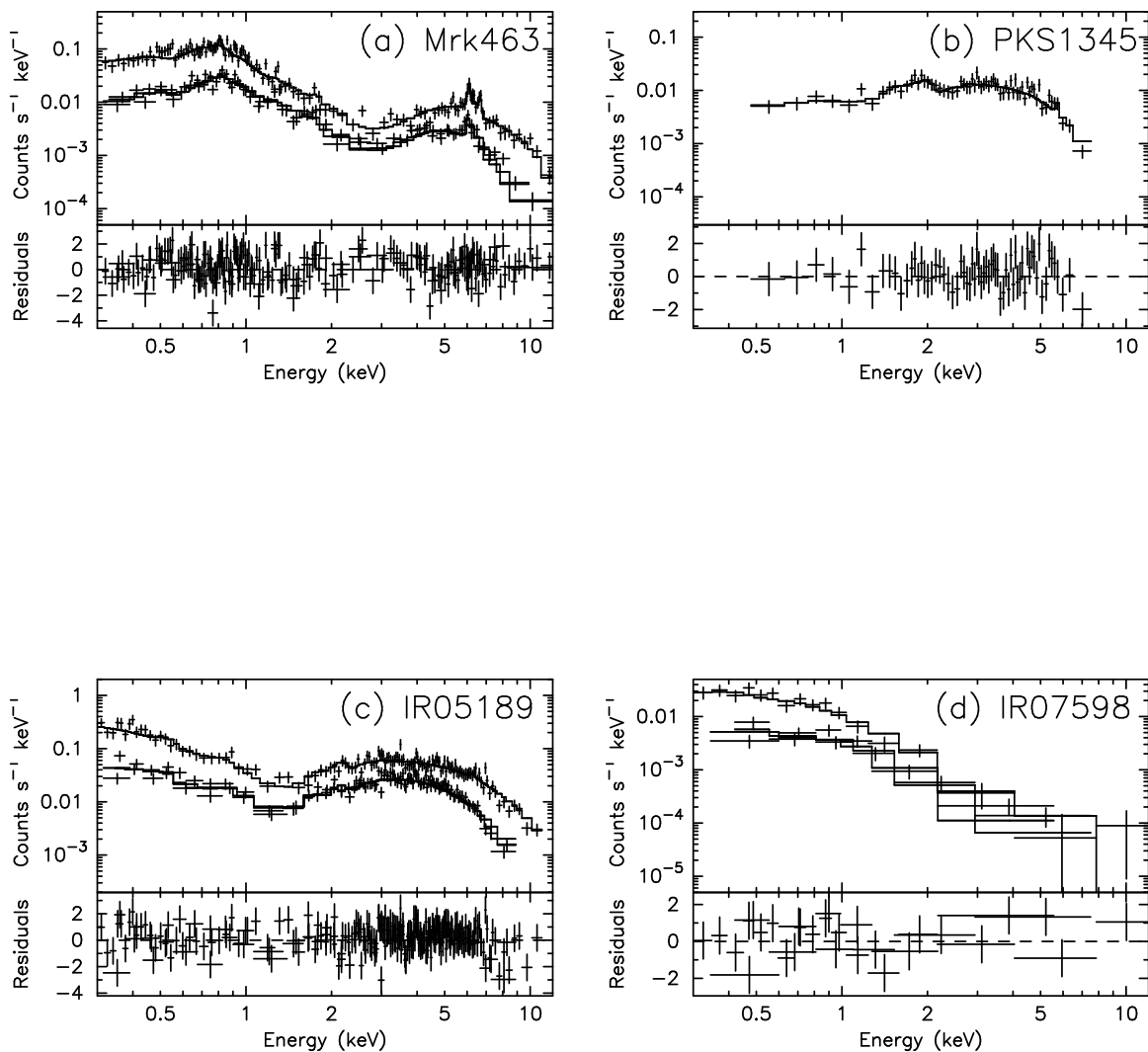


Fig. 2.— (a): An *XMM* spectrum of Mrk 463. Model A is overplotted as solid lines. In the upper panel, the higher plots are a PN spectrum (which contains the most counts), and the lower plots are MOS spectra. The lower panel shows residuals of data from the model. (b): A *Chandra* spectrum of PKS 1345+12. Model C is overplotted. (c): An *XMM* spectrum of IRAS 05189–2524. Model D is overplotted. (d): An *XMM* spectrum of IRAS 07598+6508. Model F is overplotted.

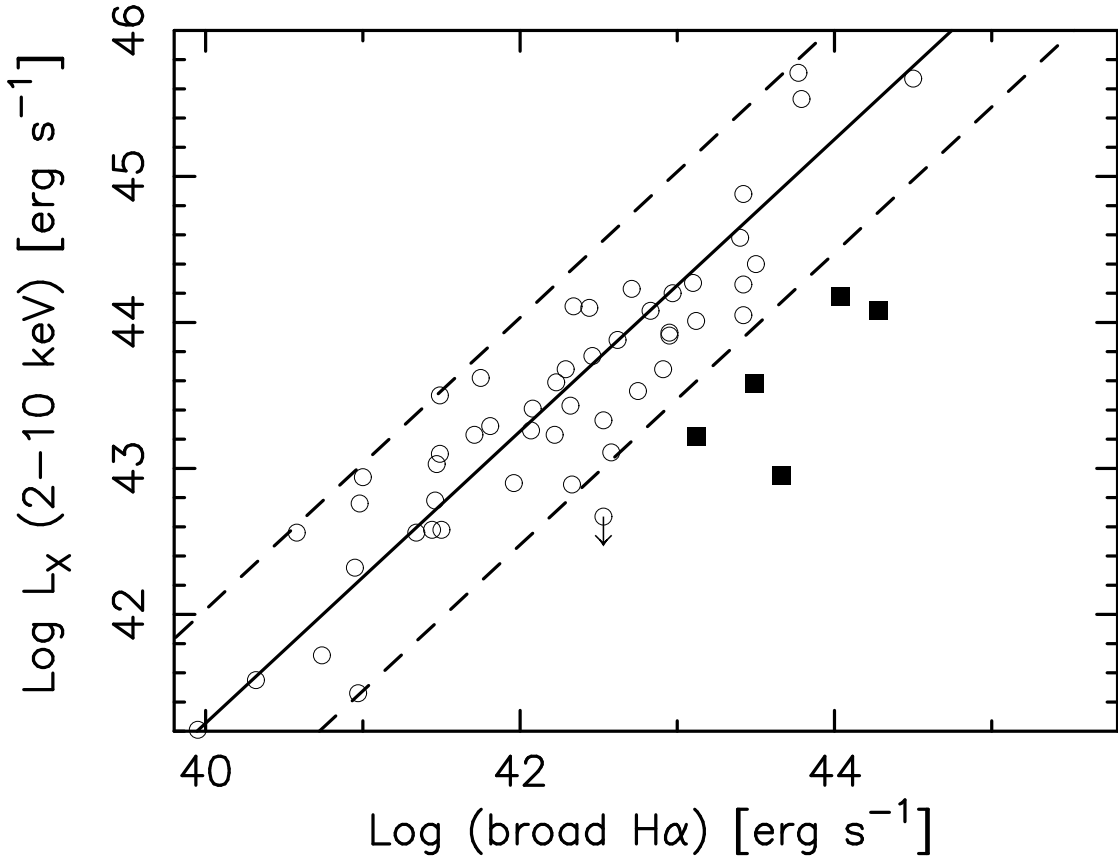


Fig. 3.— Absorption-corrected 2–10 keV X-ray luminosity (ordinate) and extinction-uncorrected broad  $\text{H}\alpha$  emission line luminosity (abscissa). Open circles are dust-unobscured type-1 AGNs with moderate infrared luminosity taken from Ward et al. (1988). Filled squares are the five Seyfert-2 ULIRGs studied in this paper, Mrk 463, PKS 1345+12, IRAS 05189–2524, IRAS 20460+1925, and IRAS 23060+0505 (see text). The solid line is for  $\log L_x(2-10 \text{ keV}) = \log L(\text{broad H}\alpha) + 1.255$  (Imanishi & Ueno 1999a). In the dashed lines,  $L_x(2-10 \text{ keV})$ -to- $L(\text{broad H}\alpha)$  ratio is a factor of 6 larger and smaller than the solid line. The only X-ray underluminous AGN (IRAS 05218–1212) originally found by Ward et al. (1988) is infrared selected by *IRAS*, if not a ULIRG. Since no information on  $\text{EW}_{6.4}$  is available, the weak 2–10 keV X-ray emission might be caused by Compton-thick absorption.